

Full Research Paper

Improvement of Flame-made ZnO Nanoparticulate Thick Film Morphology for Ethanol Sensing

Chaikarn Liewhiran^{1,2} and **Sukon Phanichphant**^{2,*}

¹ Department of Physics, Faculty of Science, Chiang Mai University, Chiang Mai 50200, Thailand.

² Nanoscience Research Laboratory, Department of Chemistry, Faculty of Science, Chiang Mai University, Chiang Mai 50200, Thailand

* Author to whom correspondence should be addressed: sphanichphant@yahoo.com

Received: 19 April 2007 / Accepted: 11 May 2007 / Published: 15 May 2007

Abstract: ZnO nanoparticles were produced by flame spray pyrolysis using zinc naphthenate as a precursor dissolved in toluene/acetonitrile (80/20 vol%). The particles properties were analyzed by XRD, BET. The ZnO particle size and morphology was observed by SEM and HR-TEM revealing spheroidal, hexagonal, and rod-like morphologies. The crystallite sizes of ZnO spheroidal and hexagonal particles ranged from 10-20 nm. ZnO nanorods were ranged from 10-20 nm in width and 20-50 nm in length. Sensing films were produced by mixing the nanoparticles into an organic paste composed of terpeneol and ethyl cellulose as a vehicle binder. The paste was doctor-bladed onto Al₂O₃ substrates interdigitated with Au electrodes. The morphology of the sensing films was analyzed by optical microscopy and SEM analysis. Cracking of the sensing films during annealing process was improved by varying the heating conditions. The gas sensing of ethanol (25-250 ppm) was studied at 400 °C in dry air containing SiC as the fluidized particles. The oxidation of ethanol on the surface of the semiconductor was confirmed by mass spectroscopy (MS). The effect of micro-cracks was quantitatively accounted for as a provider of extra exposed edges. The sensitivity decreased notably with increasing crack of sensing films. It can be observed that crack widths were reduced with decreasing heating rates. Crack-free of thick (5 μm) ZnO films evidently showed higher sensor signal and faster response times (within seconds) than cracked sensor. The sensor signal increased and the response time decreased with increasing ethanol concentration.

Keywords: ZnO, Flame spray pyrolysis, Crack, Ethanol sensor.

1. Introduction

In the field of gas sensors, it is well known that ethanol vapor is one of the most exhaustively studied gases. Metal oxide semiconductor, usually representing a property that the electrical conductivity varies with the composition of the gas atmosphere surrounding it is a popular and useful sensing material for ethanol vapor sensing. Many researchers have developed ethanol vapor sensors based on semiconductor metal oxide. Several oxide materials commonly used as ethanol gas sensors including pure and metal-doped e.g. SnO₂ [1-11], In₂O₃ [12, 13], TiO₂ [8, 14-19], ZrO₂ [8], WO₃ [7, 18], MoO₃ [18], Cu₂O [20], and ZnO [21-54], especially ZnO is known to be one of the earliest discovered and the most widely applied oxide gas sensing material.

Zinc oxide (ZnO) is an *n*-type semiconductor of wurtzite structure, with a direct large-band gap of about 3.37 eV at low temperature and 3.30 eV at room temperature [54-56]. It is sensitive to many sorts of gases at moderate temperature, especially for ethanol vapor [21-54]. ZnO is one of the most widely applied oxide-gas sensor. ZnO gas sensing materials owe to their high chemical stability, low cost, and good flexibility in fabrication. ZnO sensor elements have been fabricated in various forms including single crystal [21, 24, 25, 53], sinter pellet [27, 30, 31], thin film [23, 34, 38-40, 44, 45, 47], and thick film [22, 46, 49, 54]. The gas sensing mechanism involves chemisorptions of oxygen on the oxide surface followed by charge transfer during the reaction between chemisorbed oxygen reducing and target gas molecules. However, the physical and sensing properties of semiconductor gas sensors are directly related to their preparation e.g. particle size, sensing film morphology, and film thickness [57-66] as well as sensing film characteristics.

Flame aerosol technology is the key process for large-scale production of nano-structured materials such as carbon blacks, fumed SiO₂ and TiO₂ and to a lesser extent, for specialty chemicals such as Al₂O₃ and ZnO powders. Flame aerosol synthesis is a cost-effective and versatile process for controlled production of nanoparticles. Flame spray pyrolysis (FSP) process was systematically investigated using an external-mixing gas-assisted atomizer supported by premixed methane and oxygen flamelets [67, 68]. In flame reactors, the energy of flame is used to drive chemical reactions of precursors resulting in clusters which further grow to nanoparticles by surface growth and/or coagulation and coalescence at high temperature [69]. The advantage of FSP include the ability to dissolve the precursor directly in the fuel, simplicity of introduction of the precursor into the hot reaction zone (e.g. a flame), and flexibility in using the high-velocity spray jet for rapid quenching of aerosol formation. In general, a flame is used to force chemical reactions of precursor compounds, finally resulting in the formation of clusters, which increase their size to a range of some nanometers by coagulation and sintering. Finally, the nanostructured powders are collected on a filter [70, 71]. Moreover, at low oxidant flow rates, the specific surface area increased with increasing oxidant flow rate as the spray flame length was reduced, leading to shorter residence time and allowing less time for particle growth. Using oxygen as oxidant the droplets burn much faster than in air, thus, product particles experience longer residence times at higher temperature [70, 72]. The effect of solution feed rate on particles specific surface area and crystalline size was also investigated [73]. The solution feed rate increased the flame height, and

therefore coalescence was enhanced, resulting in large primary particles [73]. Furthermore, the flame conditions can be used to control the morphology of particles. ZnO nanorods formation were produced by FSP, which was described by XRD lattice aspect ratio [74, 75].

Many researchers reported that pure ZnO [21-27] and metal-doped ZnO [28-36] were widely used to detect ethanol vapor. For examples, ZnO thin films were produced by spray pyrolysis [23]. Film layers of 20 μm in thickness showed sensor signal in terms of rather high ethanol concentration (1000-5000 ppm) at 150-350°C. At high operating temperature, they did not depend on the concentration of ethanol [23]. An ethanol sensor based on ZnO nanorods prepared by hydrothermal method [24] showed high sensitivity to ethanol concentration ranging from 10 to 2000 ppm at 330°C, with good response and recovery time. Furthermore, ZnO nanowire ethanol gas sensor showed high sensor signal and fast response to ethanol gas at concentration up to 200 ppm with operating temperature of 300°C [25]. In addition, pure ZnO nanorods and nano-needles produced by hybrid induction and laser heating (HILH) technique also showed capability to produce sensors with good sensor signal at a maximum temperature around 400°C for a concentration of 100 ppm of volatile organic compounds (VOCs) including acetone, toluene, and ethanol. 4.58 at% In/ZnO showed highest sensor signal compared to pure ZnO [29]. Also Al/ZnO thin films were prepared by RF magnetron sputtering on Si substrate using Pt as interdigitated electrodes. The gas sensing results showed that the sensor signal for detection 400 ppm ethanol vapor was about 20 at an operating temperature of 250 °C [38]. Therefore it is interesting to apply FSP for production of ZnO nanoparticles [72-73] as used in gas sensor of ethanol vapor.

Many researchers mentioned a variety of techniques used to prepare the sensing films, i.e. plasma enhanced chemical vapor deposition (PECVD) [39], spray pyrolysis [23, 39], screen printing [49, 62], dip-coating [14, 40], and doctor-blade [54, 76, 77]. Particularly, doctor-blade technique has several advantages in producing the sensing thick films suitable for the gas sensor including relatively homogeneous composition, regularities in the film thickness, and easy control of film thickness. Therefore, it is important to investigate the most suitable thickness and sensing surface for the ethanol sensor based on flame-made ZnO nanoparticles.

Cracking formation phenomenon is one of the most serious problems when physical properties changes; film thickness [54, 65, 66, 78] were formed on substrate with different thermal expansion coefficient from the film [79-82]. The heating rates were too fast to form the cracks in the thick film [83]. Annealing of films is also of relevance to the general problem of constrained annealing [84]. Damage during constrained annealing typically begins in the early stages of densification and near preexisting defects. It can be in the form of macroscopic cracks, diffuse damage, or a combination of the two. Therefore, crack-free thin film sensing layer should show a good sensing behavior of sensor materials based on flame-made ZnO nanoparticles.

2. Experimental

2.1. Flame-made ZnO Nanoparticles

Precursor solutions (0.5 M) were prepared by dissolving appropriate amounts of zinc naphthenate (Strem, 10 wt% Zn) in toluene (Riedel deHaen, 99.5%)/acetonitrile (Fluka, 99.5%) mixtures with ratio of 80/20 vol%. In a typical run, the as-prepared precursor mixture was fed into a nozzle at a constant feed rate of 5 ml/min using a syringe pump (Inotech). At the end of the nozzle the precursor solution was dispersed by 5 ml/min oxygen forming a spray with a pressure drop at the capillary tip kept constant at 1.5 bars by adjusting the orifice gap area. This flame conditions will be depicted as 5/5 flame. The spray was ignited by supporting flamelets fed with oxygen (2.4 l/min) and methane (1.13 l/min) which are positioned in a ring around the nozzle outlet. The flame height was 10 cm and showed a yellowish-orange flame appearance as shown in the inset. After evaporation and combustion of precursor droplets, particles are formed by nucleation, condensation, coagulation and coalescence. Finally, the nanoparticles were collected on a glass microfibre filters (Whatmann GF/A, 25.7 cm in diameter) with the aid of a vacuum pump. The flame made (5/5) ZnO as-prepared nanopowders were designated as P0.

2.2. Particle Characterization

X-ray diffraction (XRD) patterns of the powder as-prepared and sensing film were obtained with a Bruker AXS D8 Advance diffractometer (40 kV, 40 mA, Karlsruhe, Germany) operating with $\text{CuK}\alpha$ radiation at $2\theta = 20\text{--}80^\circ$ with a step size of 0.06° and a scanning speed of $0.72^\circ/\text{minute}$. The fundamental parameter approach and the Rietveld method [85] were applied to determine the hexagonal phase and the crystallite size of nanopowder. The phase and the corresponding sizes were calculated using the software TOPAS-3. The specific surface areas of ZnO nanoparticles was determined with the 5-point nitrogen adsorption measurement applying the Brunauer-Emmett-Teller (BET) method [86] at 77 K (Micromeritics Tristar 3000). All samples were degassed at 150°C for 1 h prior to analysis. The diameter of particles can be calculated by $d_{\text{BET}} = 6 / \text{SSA}_{\text{BET}} * \rho_{\text{sample}}$, where SSA_{BET} is the specific surface area (m^2/g) and ρ_{samples} is the density of ZnO ($\rho_{\text{ZnO}} = 5.61 * 10^3 \text{ kg/m}^3$) [73]. The morphologies of nanoparticles of sample P0 were observed by the scanning electron microscopy (SEM) (JSM-6335F, JEOL) and high-resolution transmission electron microscopy (HR-TEM) using the Tecanai 30F microscope (Philips; field emission cathode, operated at 300 kV) and JSM-2010, JEOL. The HR-TEM bright-field images were obtained using a slow-scan CCD camera.

2.3. Preparation of Sensor

2.3.1 Paste Preparation

An Al₂O₃ substrate interdigitated with Au electrodes (Au/Al₂O₃; 10 x 10 x 0.1 mm; Electronics Design Center, MicroFabrication Lab, Case Western Reserve University) was used as a sensor substrates designated as A0. An appropriate quantity of 0.28 ml homogeneous mixed solution was prepared by stirring of ethyl cellulose (Fluka, 30-60 mPa.s) as the temporary binder and terpineol (Aldrich, 90%) as a solvent with a mixing ratio of 480 mg to 18 g. The viscous mixture was combined with 70 mg of samples P0 and mixed to form a paste for 30 min prior to doctor-blade.

2.3.2 Cracking Improvement and Sensing Surface Characterizations

Fig. 1 and Table 1 show the heating conditions (HC), which varied to improve crack formation and crack width. With the influence of HC, all sensor substrates samples were doctor-bladed and annealed continuously at 50, 75, 100°C with the rate varied to 0.5, 1, 2, 5, 10, 20°C/min for 1 h, and kept constant at 400°C with the rate of 2°C/min for 2 h by annealing the appropriate temperature for complete binder removal [62, 87-90], and then subsequently cooled down to 20°C with the rate of 5°C/min. The various HC were designated as HC1, HC2, HC3, HC4, HC5, and HC6, respectively. Finally, an optical surface analysis in terms of a surface morphology and cracking phenomenon was performed using a microscope with an UV-source (Zeiss Axioplan 2[@]; Carl Zeiss, Germany). Images were processed using Zeiss Axio version and applicable AxioCam MRc.

2.3.3 Doctor-bladed Thick Film Preparation

A schematic of doctor-blade processing used to fabricate the sensor which involves smearing the paste across the template, removing the resist and annealing the paste, was shown in Fig. 2. The resulting paste doctor-bladed on the Al₂O₃ substrates interdigitated with Au electrodes were prepared [76, 77]. All substrates were taped (Scotch MagicTM tape; Art. Nr.11110300, Ethilux, Germany) upon the edges for 1 tape which control the film thickness to be approximately 5 μm prior to doctor-blade. We believe that the tape plays an important role in controlling the thick films layer by providing a template for film thickness formation (1 tape can control thickness approximately 5 μm). The resulting substrates were heated in an oven in the same conditions of HC1 and HC6 prior to sensing test. The crack-free and the most crack sensor were obtained. Finally, the gold bonding was fabricated using pure gold wires (Alfa Aesar, 0.2 mm (0.008in) dia, 99.9% (metal basis)) that were put through the tiny holes of gold electrodes by soldering.

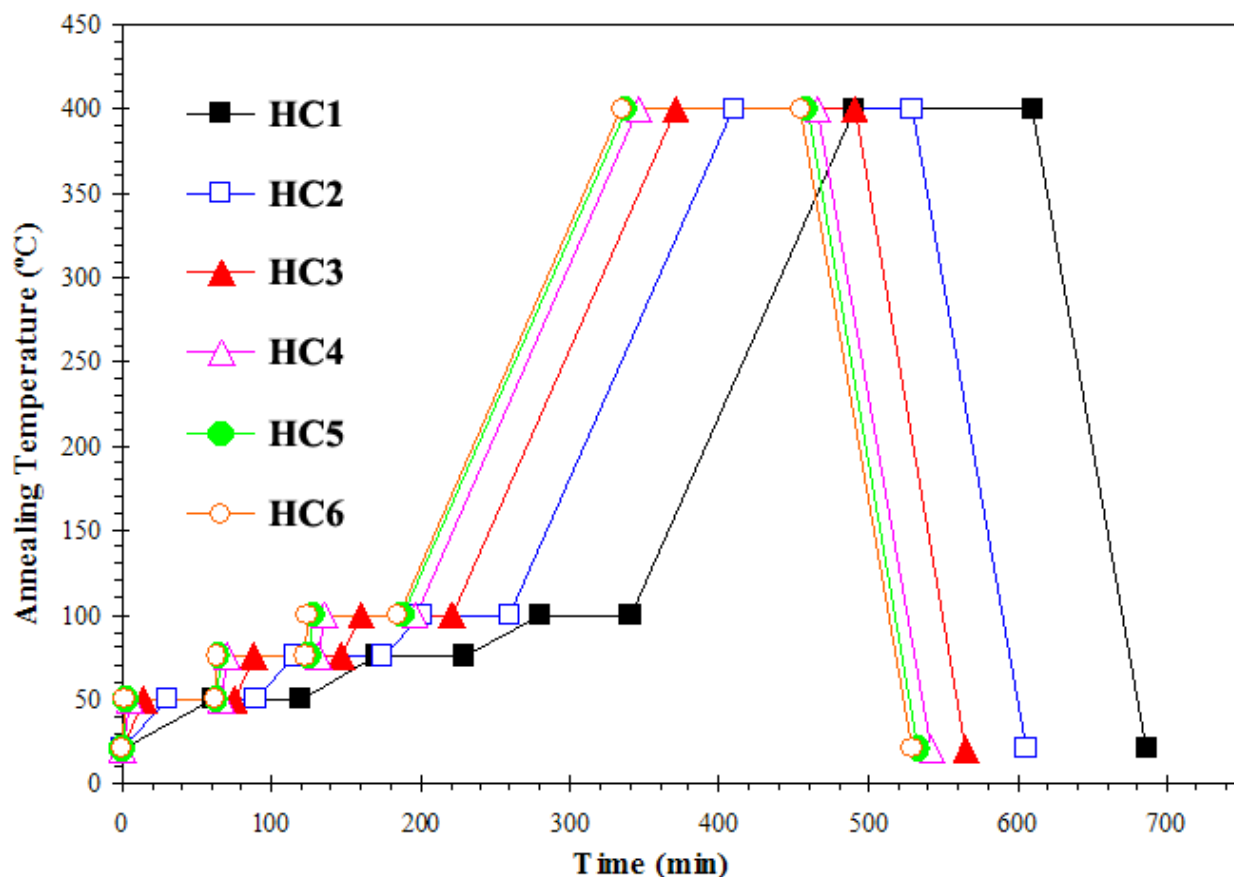


Figure 1. Diagram of heating conditions (HC) during film preparation for improvement of cracking.

Table 1. Cracking sensing layer improvement heating conditions.

Samples	Heating Conditions (HC)							
	Annealing temperatures & Heating rates							
	50 °C		75 °C		100 °C		400 °C	
	rate (°C/min)	time (min)	rate (°C/min)	time (min)	rate (°C/min)	time (min)	rate (°C/min)	time (min)
HC1	0.5	60	0.5	60	0.5	60	2.0	120
HC2	1.0	60	1.0	60	1.0	60	2.0	120
HC3	2.0	60	2.0	60	2.0	60	2.0	120
HC4	5.0	60	5.0	60	5.0	60	2.0	120
HC5	10.0	60	10.0	60	10.0	60	2.0	120
HC6	20.0	60	20.0	60	20.0	60	2.0	120

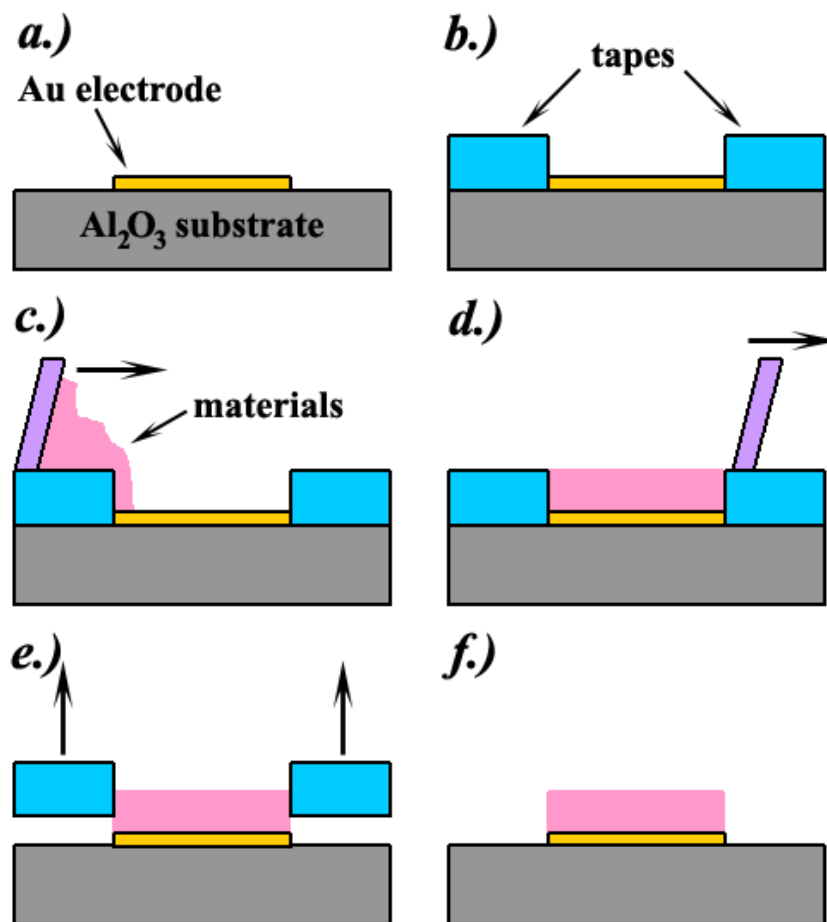


Figure 2. Doctor-blade process of sample onto the template. (a) Au/Al₂O₃ substrate, (b) tape with patterned templates, (c) doctor-blade sample paste across template, (d) patterned features, (e) removing the tapes, and (f) annealing the paste.

2.4. Characterization of Gas Sensing Properties and Mass Spectrometry Measurements

The sensor measurement has been performed to monitor the response to ethanol (25-250 ppm) in dry air N₂/O₂ atmosphere. The pulse time of the gas at each concentration was usually 180 s. A schematic of the sensor experimental set up was shown in Fig. 3. The sensor samples were placed in the center of quartz tube (3 cm diameter and 60 cm length) containing SiC as the fluidized particles (1/2 of quartz tube length), which in turn was introduced into a tubular oven (Nabertherm Controller P320, Germany). The vibrating fluidized bed (VFB) has been applied commercially to various processes, such as heat exchange, particle processing and chemical reaction, etc. The mechanical vibration imposed on a fluidized bed can significantly improve gas-solid contact and gas transport characteristics [91, 92]. Gold wires were soldered to the sensor Au electrodes externally connected with a digital multimeter (KEITHLEY model 2700 DMM, Germany) to record the sensor resistance. The furnace was heated to 400 °C and kept at this temperature during the sensor test. The total gas flow rate of 2

l/min was passed through the quartz tube and controlled by mass flow controllers (Bronkhorst HITEC, Germany). By monitoring the output voltage across the sensor, as the operating temperature increased up to 400°C, the resistances of the sensor in dry air and in test gas were alternately increased and decreased. The analyte ethanol gas adsorbs on the ZnO sensing layer and causes a change in resistance depending on the gas concentration. This is monitored by a digital multimeter connected to the sensor substrate with Au wires. The measurement was done in 21% accompanying O₂ and 0% H₂O with 79% N₂. The sensors were allowed to stabilize for at least 1 h at the operating temperature (400 °C) and N₂/O₂ flow. The sensor signal, S is defined in the following as the resistance ratio R_a/R_g for the reducing gas (ethanol) [24, 29], where R_a is the resistance in dry air, and R_g is the resistance in test gas. The response time, T_{res} is defined as the time required until 90 % of the response signal is reached. The recovery times, T_{rec} denotes the time needed until 90 % of the original baseline signal is recovered. Moreover, the sensor experimental set up was applicably connected with mass spectrometer (MS) for ethanol sensing interaction with oxygen on the surface of semiconductor material measurement. After annealing and sensing test of sensors fabricated using samples P0 with controlled the sensing film thickness and sensing layer morphology using the HC1 and HC6, they were designated as S1 and S6, respectively. Finally, all sensing layers morphologies were analyzed by SEM analysis.

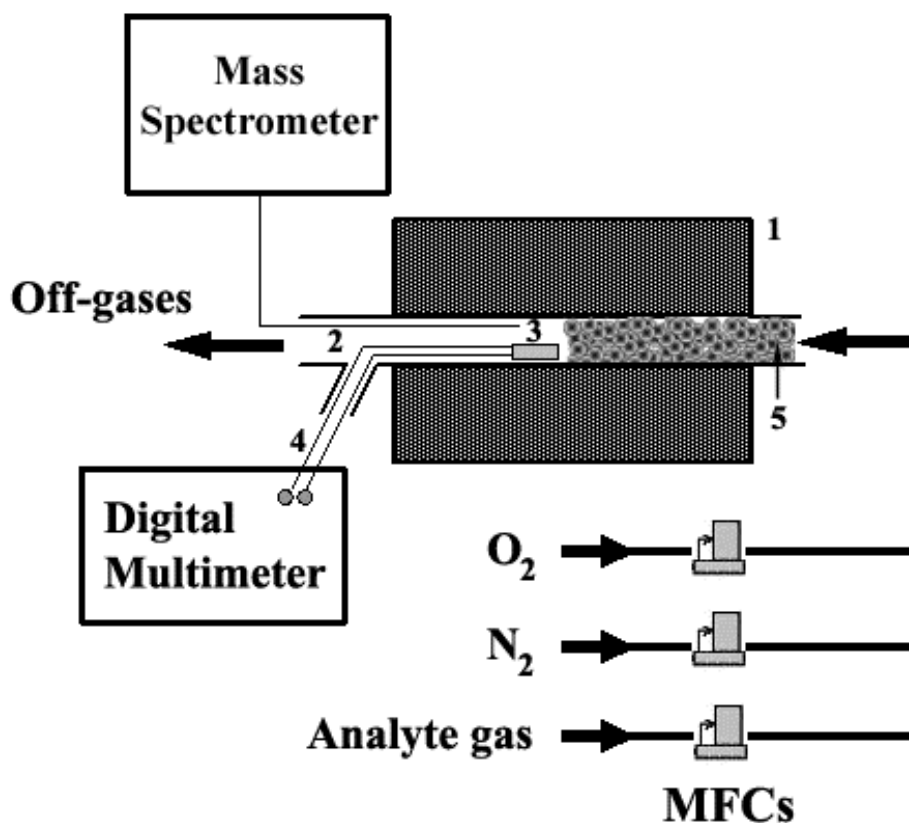


Figure 3. Schematic of the experimental set up for sensor evaluation with the tube furnace (1), the quartz tube (2), the sensor (3), the gold wiring (4), and the fluidized SiC particles (5).

3. Results and Discussion

3.1. Particles Properties

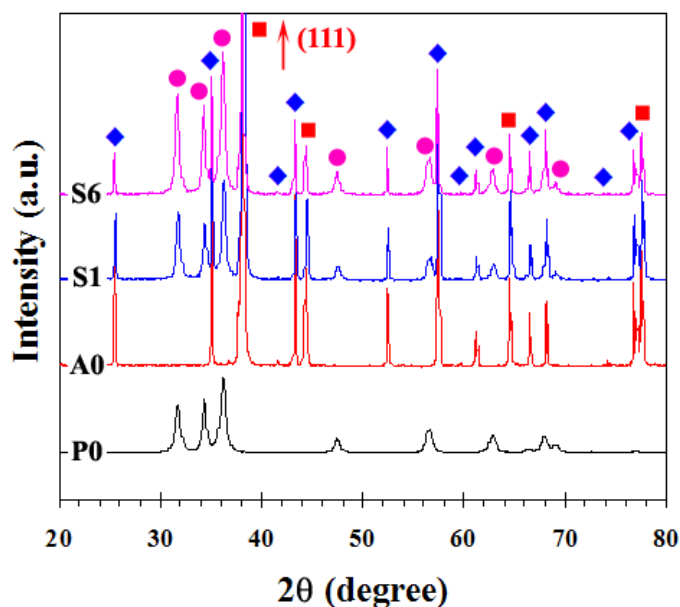


Figure 4. XRD patterns of flame-made (5/5) ZnO as-prepared (P0), Al₂O₃ substrate interdigitated with Au electrodes (A0), crack-free (S1) and the most crack sensor (S6) after annealing and sensing test at 400°C ((●) ZnO; (■) Au; (◆) Al₂O₃).

Fig. 4 shows the XRD patterns of samples as-prepared (P0), Au/Al₂O₃ substrate (A0), crack-free (S1) and the most cracked sensors (S6) after annealing and sensing test at 400°C. The samples P0 were highly crystalline, and all peaks can be confirmed to be a hexagonal structure of ZnO (Inorganic Crystal Structure Database [ICSD] Coll. Code: 067454 [93]), which matches well with the model by Abrahams et al. [94]. The diffraction peaks were slightly sharp for sensor samples S1 and S6 as compared to sample P0, suggesting relatively larger particles during the resistance stabilization and sensing test. The diffraction patterns of Al₂O₃ (modified structural parameters of ICSD Coll. Code: No. 085137 [95]) (filled diamonds) and Au (modified structural parameters of ICSD Coll. CAS No. 7440-57-5 [96]) (filled rectangular) from the substrates are also visible in the A0, S1 and S6, especially, the sensors S1 and S6 showed ZnO peaks (filled circles), which confirm the ZnO thick film sensing layer doctor-bladed on Au/Al₂O₃ substrates. Also the Au (111) peak showed the strongest peak in terms of intensity. The average crystal sizes (d_{XRD} ave.) were calculated by the fundamental parameter approach Rietveld method [85] based on the half-maximum widths of Sherrer's equation [97] to compare with the average BET-equivalent particle diameter (d_{BET}). The diffraction peaks were slightly sharp for sensor S1 and S6 after sensing test at 400°C as compared to sample P0 (P0, SSA=63.8 m²/g, d_{BET} =16.8

nm, d_{XRD} ave.=18.3 nm). Nevertheless, accurate particles size, the morphology of nanoparticles, and elemental compositions can be confirmed by TEM bright-field images and EDS analyses.

Fig. 5 shows SEM images of highly crystalline flame-made (5/5) ZnO nanoparticles at low magnification. The flame-made ZnO nanoparticles showed rather dispersion of particles, with diameters ranging from 10–20 nm. While the SEM images provide 3-D morphology and estimated particle sizes, TEM images can reveal internal structure and a more accurate measurement of particle size and morphology.

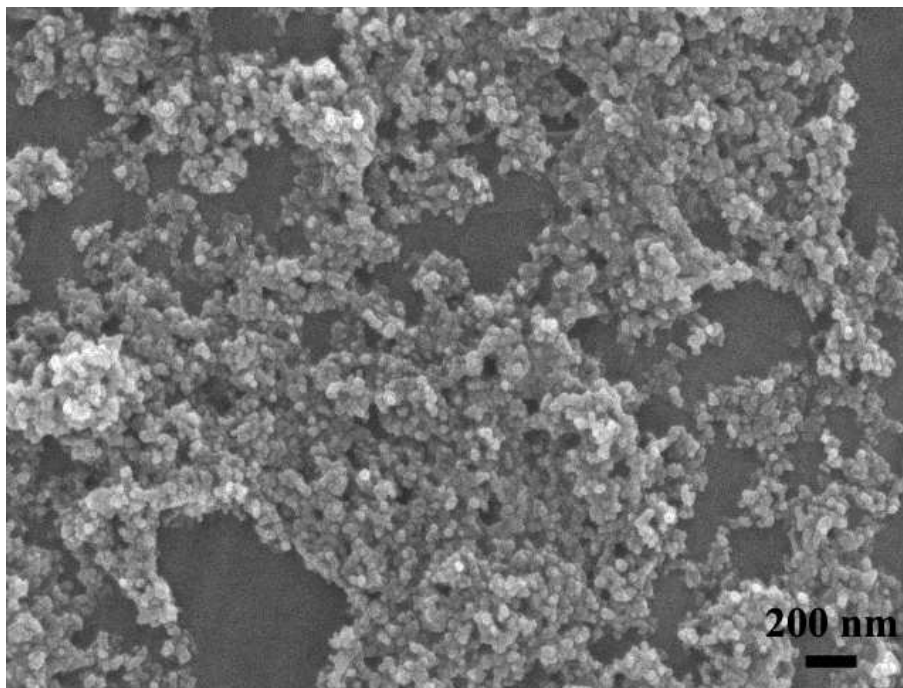


Figure 5. SEM image of highly crystalline flame-made (5/5) ZnO nanoparticles.

Fig. 6 (a) and (b) show the bright-field TEM images of samples P0 observed at the different magnifications. The corresponding diffraction patterns are shown in the insets. The diffraction patterns illustrating spot patterns of the hexagonal structure of ZnO indicated that the ZnO nanoparticles are highly crystalline, which is in good agreement with the XRD data. The flame-made ZnO nanoparticles can be observed as particles having the clear rod-like, hexagonal, and spheroidal shapes. Fig. 6 (a) and 6 (b) shows the morphologies of flame made (5/5) ZnO nanoparticle containing mainly spheroidal particles typically with diameters ranging from 10-20 nm with occasional hexagonal and rod-like particles. The crystalline sizes of ZnO hexagonal particles were in the range of 10-20 nm, and nanorod-like particles were in the range of 10-20 nm in width, 20-50 nm in length. This is consistent with Tani et al. [73] and Height et al. [74, 75]. Fig. 6 (c), and (d) gave the EDS elemental compositions signals associated with regions as indicated. EDS 1 and EDS 2 emphasized the signals for Fig. 6 (a) and (b) corresponding to Zn and O, while Cu and C caused by the contamination from the copper grid coated with carbon.

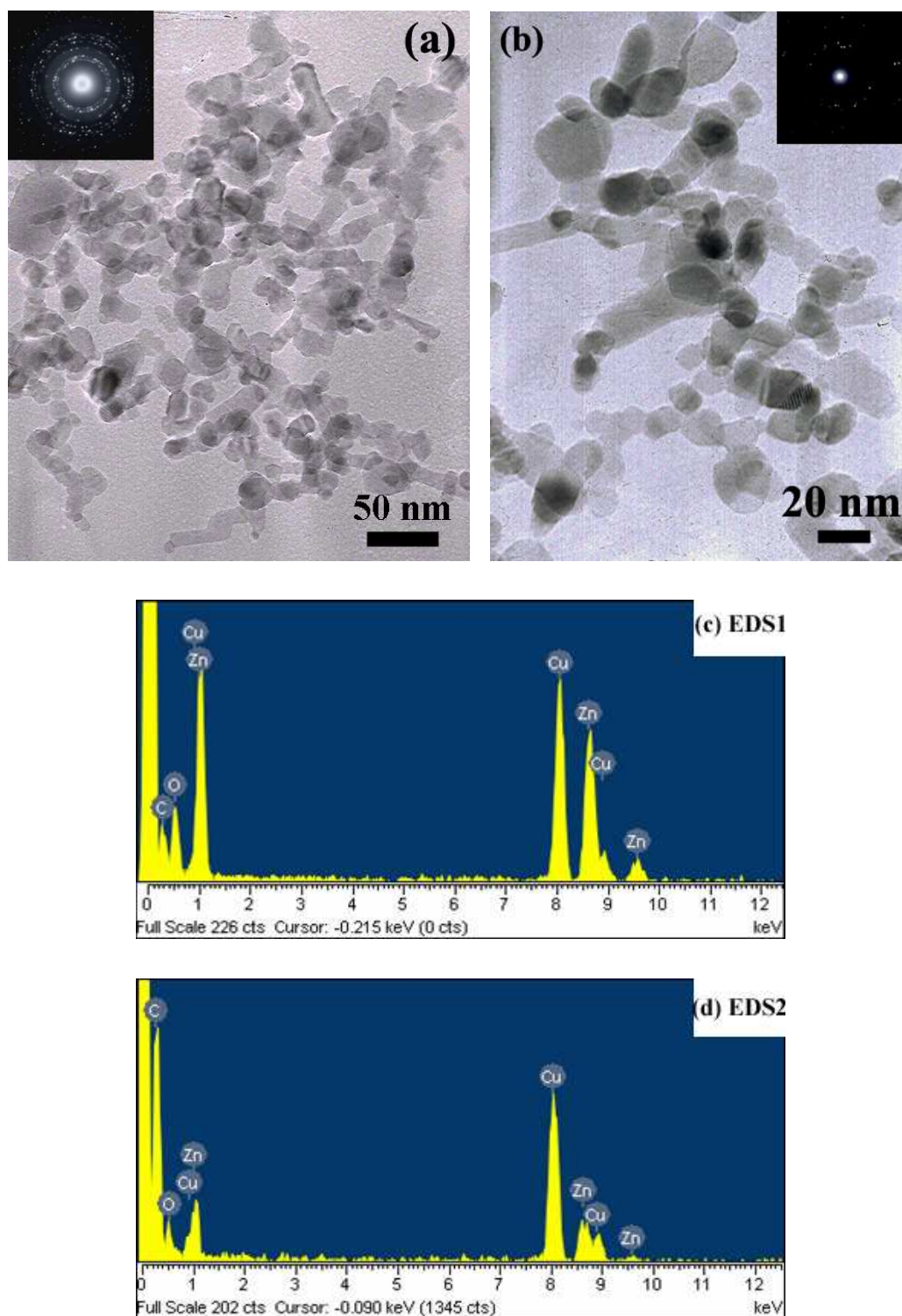


Figure 6 (a, b) HR-TEM bright-fields image of highly crystalline flame-made (5/5) ZnO nanoparticles with different magnifications. The morphologies can be observed (a, b) mainly spheroidal particles typically with occasional hexagonal and rod-like particles. Insets show the corresponding diffraction patterns of the particles. (c, d) EDS spectra for Fig. 6 (a) and (b) corresponding to Zn and O, while Cu and C caused by the contamination from the copper grid coated with carbon.

3.2. Cracking thick film sensing layer improvement

3.2.1. Influence of heating rate

Many factors can affect crack formation including binder removal, heating rate, temperature, and time. Cracks formation usually results from inhomogeneities in the green body. Often, cracks that appear in annealing are carried over from shaping operations but are enlarged during annealing. Even in this simple case the annealing shrinkage depends on several factors: green density, particle sizes, mixture composition, and mixture homogeneity. For mixed-powder systems, the homogeneity of the powders is a major factor. The distribution of the additive improves as its particle size decreases, and mixing prior to compaction is often beneficial. Moreover, for the powder formed by binder-assisted technique, when it was heat up to the burnt out temperature, the binder removal could be performed. The stresses associated with compact shrinkage during annealing often are near the annealing stress. When the annealing stress and flaw join together, a critical condition can arise where the stress concentration at the flaw exceeds the compact strength. This leads to flaw growth, just as a crack formation easily through any material. Crack in the green body enlarge during annealing. The annealing process is an important aspect to heating. The compact exterior of particles caused by heating, initial melting at the surface, the circumferential shrinkage stresses, and binder removal lead to the cracking of the component if the heating rate is too rapid [83, 84, 98]. Once a melt was formed at the compact surface, it flows into the interparticle pores and subsequently can penetrate the grain boundaries in the particles. Thus, the heating rate is an essential part in controlling the microstructure evaluation in the annealing process. The influence of heating rate can be clearly seen in Fig. 7 (a-f). It was found that sample annealed using a HC1 showed crack-free formation and regular surface. Crack width evidently increased with increasing the HC as seen in HC2 to HC6. Several cracking phenomena were proposed such as the large polycrystalline grains were formed by necking and merging of small grains during the annealing process. The cracks between large grains were formed when the small grains become closer and agglomerated during the heating process and shrinkage occurred during the cooling process. When the heating rate was very slow (0.5°C/min) the crack-free film was formed and showed significant difference compared to different heating rates. On the other hand, when the heating rate was very fast (20°C/min) crack formation were formed.

Cracks increased with increasing the heating rate during annealing process because large grains or crack gaps caused the decreasing in the surface area, connectivity of films and deteriorating film properties of the electronic materials. Fig. 8 shows how the morphology changes with increasing the heating rate as the same film thickness. Cracks showed up when the films shrank as a result of grain growth in the annealing process. It is suspected that the cracks do not penetrate through the film down to the bottom. Crack formation can be formed with the difference in the thermal expansion coefficient mismatch between substrate, materials. The heating rates causing these cracks were related directly to tensile stress. It has been found that the sample annealed using very fast heating rates showed more cracks than slower heating rates [83, 84].

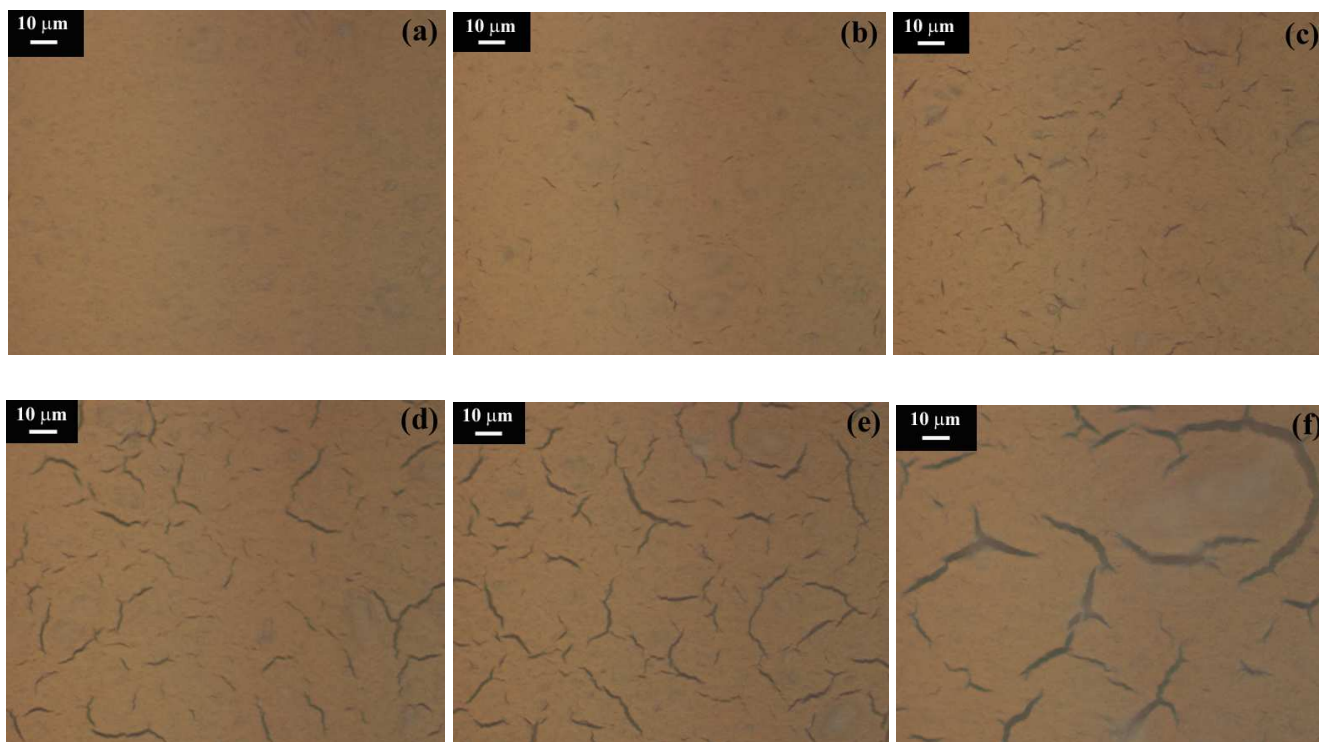


Figure 7. (magnification 50x) Crack formation in thick film sensing layers of flame-made ZnO nanoparticles treated with different heating conditions in terms of heating rates, time, and annealing temperatures (HC1-HC6 ; compared to Table 1).

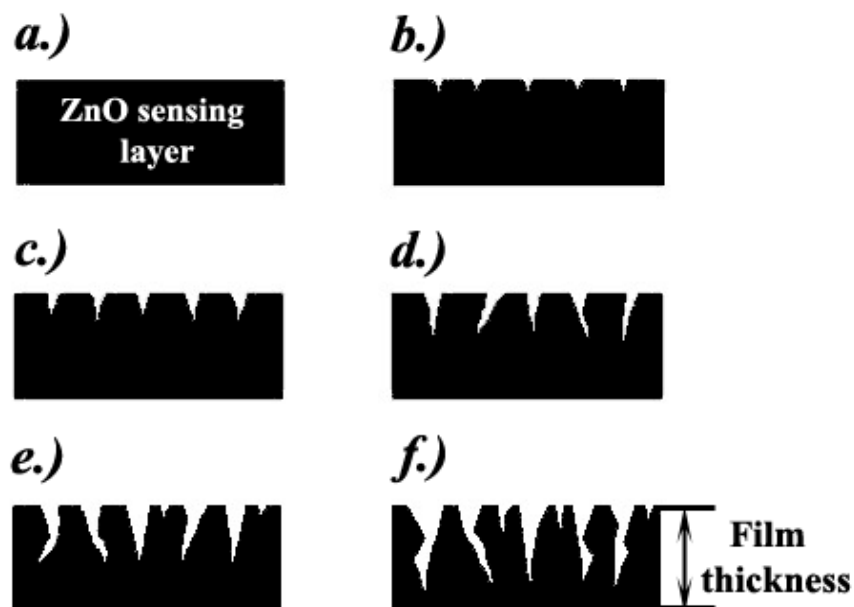


Figure 8. Model for the influence of heating condition (a) HC1, (b) HC2, (c) HC3, (d) HC4, (e) HC5, (f) HC6 in terms of annealing temperature and heating rate on sensing film morphology.

3.3. Gas Sensing Properties

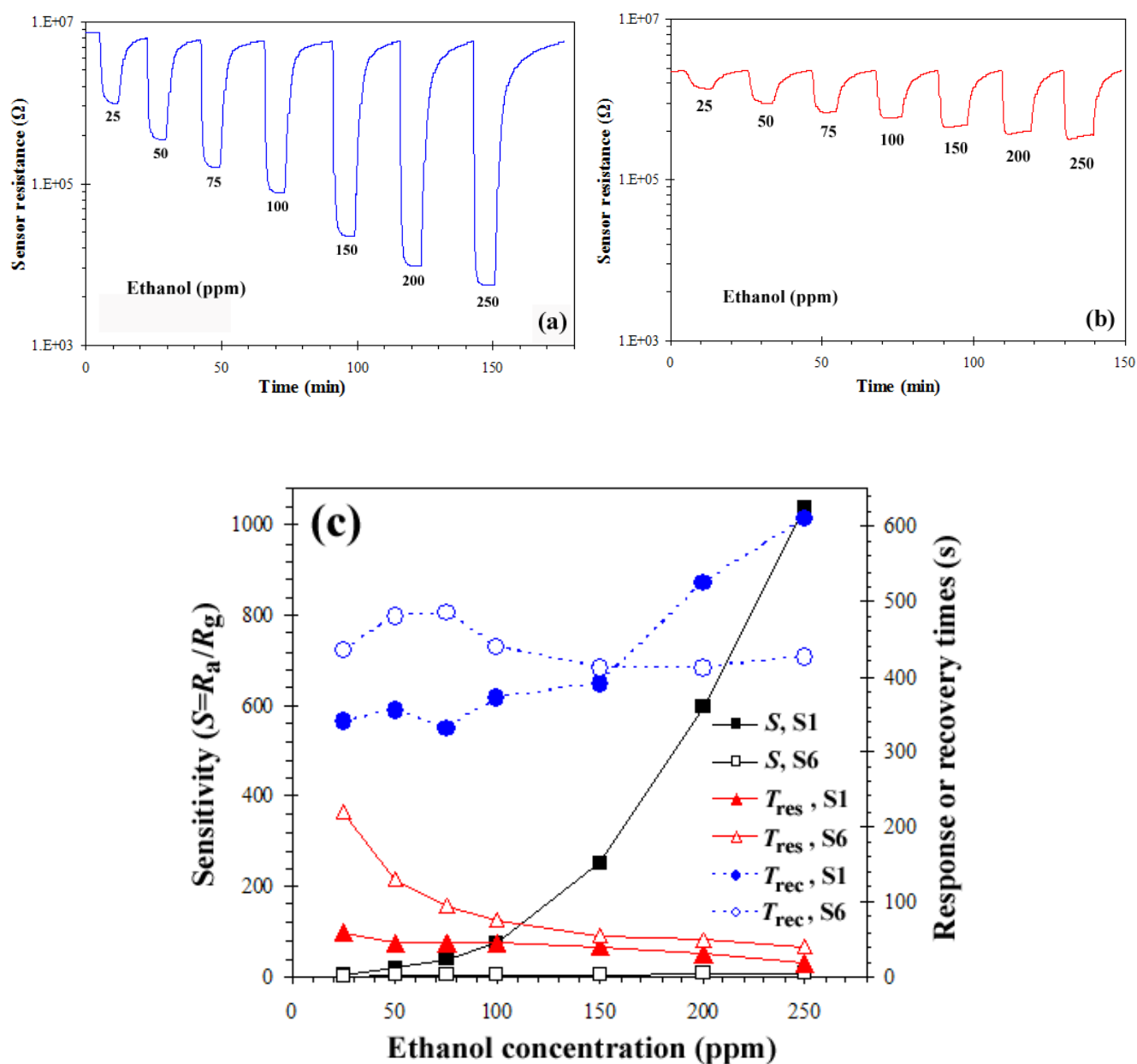


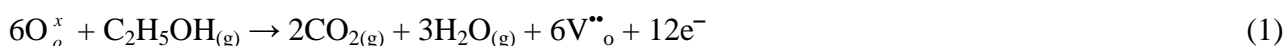
Figure 9. Change in resistance of (a) crack-free sensor S1 and (b) the most cracked sensor S6 under exposure to reducing gas ethanol during forward cycle, and (c) the plot of sensor signal of S1 and S6 (left axis) dependence on ethanol concentration and cracking phenomenon in dry air (O_2/N_2) at 400°C.

The response times (T_{res} , solid line, right axis) were within seconds, recovery times within minutes (T_{rec} , dashed line, right axis).

Fig. 9 illustrates the sensor behaviors versus the ethanol concentrations ranging from 25-250 ppm plot for the crack-free (S1) and the most cracked (S6) sensor based on an as-prepared flame-made (5/5) ZnO nanoparticles towards reducing gas ethanol at sensing operating temperature 400 °C. Zhu et al. [9] reported that the sensor signal of ZnO showed a maximum around 400 °C for all organic vapors such as acetone, benzene, ethyl alcohol etc. Better response should be expected for larger concentration of reducing gas adsorbed, because the reaction between the adsorbed reducing gas and oxygen species becomes more favorable. From this data, as the crack increases (sensor S6), it can be clearly noticed that the crack-free sensor (S1) can improve the sensor behaviors in terms of sensor signal and response times, evidently better than S6. Fig. 9 (a) shows the change in resistance of crack-free sensor S1 under exposure to ethanol at 25-250 ppm during a forward cycle. The resistance decreased drastically during the gas exposure, a typical behavior for ZnO as an n-type semiconductor [25]. The sensor S1 showed the crack-free morphology on sensing surface corresponding to the high performance and sensing behaviors in terms of sensor signal, response and recovery times. The high sensor signal of sensor S1 to 250 ppm ethanol concentration was 1038. On the other hands, the change in resistance of the most crack sensor S6 under exposure to ethanol at 25-250 ppm during a forward cycle was shown in Fig. 9 (b). The sensor signal was very low compared with sensor S1 as the same ethanol concentrations (to 250 ppm, $S=6.9$). The T_{res} was slightly sluggish. This is because the serious crack widths caused the decreasing in the surface area, connectivity of films, and deteriorating a gas sensing properties. It can be assumed that the decreasing of the sensing film surface areas (serious crack) affected to decrease the depletion layer at the surface, thus the reaction of reducing ethanol gas with the charged oxygen species destroyed the electron localization process drastically reduced and a change in conductivity was decreased. Thus, the most crack should be shown the lower sensing performance than the crack-free sensor. Fig. 9 (c) showed the plot of sensor signal of sensor S1 (filled rectangles, left axis) and S6 (open rectangles, left axis) during the forward cycle of the ethanol sensor test in Fig. 9 (a) and 9 (b). The sensor signal consistently increased with increasing ethanol concentration. The response (solid line, right axis) times of sensor S1 (fill triangles) and S6 (open triangles) and recovery time (dashed line, right axis) times of sensor S1 (fill circles) and S6 (open circles) during the forward cycle were also included in Fig. 9 (c). The response time, T_{res} , was within seconds, it slightly decreased at increasing ethanol concentrations (in the order of 10 s). T_{res} was 60 and 20 s for sensor S1 at 25 and 250 ppm, respectively. T_{res} was 220 and 40 s for sensor S6 at 25 and 250 ppm, respectively. The trend of T_{rec} was so long within minutes. Compared with the same material references reported by Liu et al. [21], these sensors produced from flame-made ZnO nanoparticles have higher sensor signal and shorter response times than those made from ZnO single crystal flakes with different sizes and morphology of particles (to 300 ppm, $S=14.3$, $T_{res}=62$ s). Also Zhu et al. [29] reported that ZnO nanorods and needle-shaped had a sensor response to 100 ppm of ethanol at 420°C of 12. Moreover, Choopun et al. [42] reported that ZnO nanobelts RF-sputtered onto a copper tube. The sensor tested at operating temperatures ranging from 200-290°C with ethanol concentration levels of 50-2000 ppm, e.g. at 220°C, when the ethanol concentration increased from 50 to 1000 ppm, the sensor signal increased from 7.3 to 23.2. In addition, Lv et al. [43] reported that the sensor fabricated from ZnO nanorods with average diameter

about 95 nm and tested at operating temperatures ranging from 150-450°C under exposure of ethanol gas. It showed the highest sensing performance (to 100 ppm, $S=120$) at 450°C. The sensor signal to 1000 ppm ethanol gas enhanced with the increasing of operating temperature from 293 to 450°C. For comparison with doping material, Zhu et al. [28] reported that the highest sensing behaviors to ethanol was at 370°C of pure ZnO (to 100 ppm, $S=15$) and ZnO incorporated with 10 wt%TiO₂ (to 100 ppm, $S=50$, and to 200 ppm, $S= 80$) sensor. Also Chou et al. [38] reported the ethanol sensing of ZnO doped with Al thin films prepared by RF magnetron sputtering on Si substrate interdigitated with Pt electrodes. The gas sensing results showed the sensor signal for detecting 400 ppm ethanol vapor was about 20 at 250°C. The response and recovery times were about 2-4 min, with good reproducibility. Comparing with different materials, Teleki et al. [14] reported the flame-made TiO₂ spherical particles film about 30 μm thick prepared by drop-coating of heptanol suspension of these powders, and the sensing test at 500°C with ethanol at concentration ranging from 10-75 ppm. A sensor showed the highest sensor signal at 75 ppm ($S=30$) in ethanol concentration. It can be clearly seen that the crack-free sensor based on high purity of flame-made ZnO nanoparticles showed very high sensor signal and also faster response time than the most cracked sensor at the highest ethanol concentration.

The interaction between the reducing gas ethanol and lattice oxygen O_o^x in a metal oxide such as ZnO can be described in general by the following defect reaction (in Kröger-Vink notation) [21]:



Similarly, the interactions between reducing gas ethanol and surface-adsorbed oxygen species [21, 31, 99] such as superoxide ion O_2^- and peroxide ion O_2^{2-} can be described as



These reactions produce more electrons and thus increase the conductivity of *n*-type semiconductor (ZnO) upon exposure to ethanol. When ZnO sensor is maintained at equilibrium at the appropriate operating temperature, oxygen in the form of oxide species like O^- , O^{2-} , O_2^- , localize mobile electrons from the *n*-type semiconducting oxide in air, creating a depletion layer at the surface of the individual particles. Thereafter, the reaction of reducing gas ethanol with the charged oxygen species destroys the electron localization process and is observed as a change in conductivity. These interactions corresponded well with the sensing reaction. Fig. 10 illustrates the characteristic MS peak intensities of interactions between reducing gas ethanol and surface-adsorbed oxygen species of ZnO sensing layer (sensor S1) including C₂H₅OH ((c) mass=46) with those of its oxidation products (CO₂ ((a) mass=44) and H₂O ((b) mass=18)) versus times at the sensing operating temperature was 400 °C. The ion intensities were shown rather strong peaks of CO₂ because CO₂ was the major product oxidized with

oxygen on the surface of semiconductor materials, which clearly related with the equations 1-3 with different oxygen species.

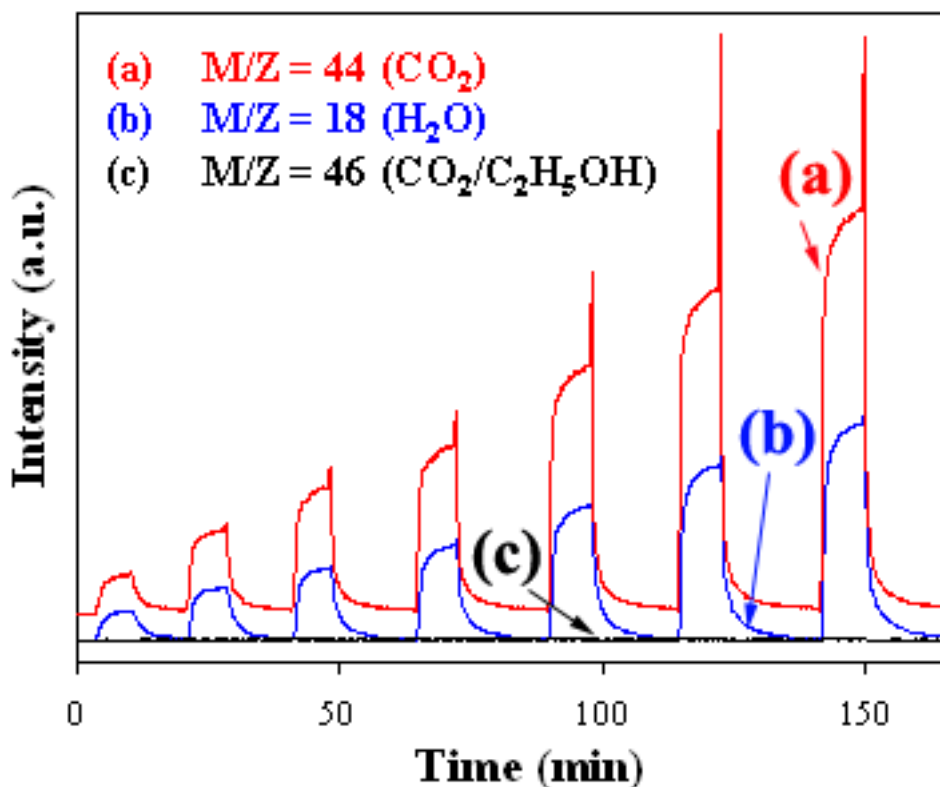


Figure 10. MS ion intensity as a function of time during ethanol oxidation in dry air at 400 °C (25-250 ppm) over a ZnO sensing film.

3.4. SEM-Cracking Sensing Layer

SEM micrographs of both the sensor S1 and S6 surface and the fracture edge were shown in Fig. 11 (a) and 11 (b). These show the crack-free and crack sensing surface of the ZnO thick film. The crack phenomenon can be described as follows. Firstly, the thermal expansion coefficients of the alumina substrate ($\sim 7 \times 10^{-6} \text{ K}^{-1}$) [80] and the ZnO ($\sim 4.75 \times 10^{-6} \text{ K}^{-1}$) [81] thick film were difference. Yamada et al. [79] mentioned that the difference in the thermal expansion of the substrate and material film was one of the most important factors responsible for the cracking phenomena. Also Deesirapipat et al. [81] reported the thermal expansion coefficient mismatch between material and substrate indicating a differential expansion coefficient probably causing these cracks. Secondly, the ZnO thick films were annealed at different annealing temperatures using very fast heating rates and cooling rates to room temperature causing a tensile stress and probably of the crack formation. This was consistent with Kono et al. [83] who reported the influence of heating rate of a gypsum investment related to cracking formation using too fast heating rate (40°C/min) compared to slower rate of 20 °C/min. Fig. 11 (a)

shows SEM images of sensor S1. It showed the crack-free of surface after annealing and sensing test. The images showed the selected regions of ZnO sensing layer indicated the size and morphology of flame-made ZnO nanoparticle. The particle sizes slightly changed after the sensing test. Surface morphology of sensor S6 investigated by SEM was shown in Fig. 11 (b). They were many large cracks on a sensing surface, and the connection between the ZnO grains layer was rather poor. The crack widths were found to be in the range of 2-5 μm .

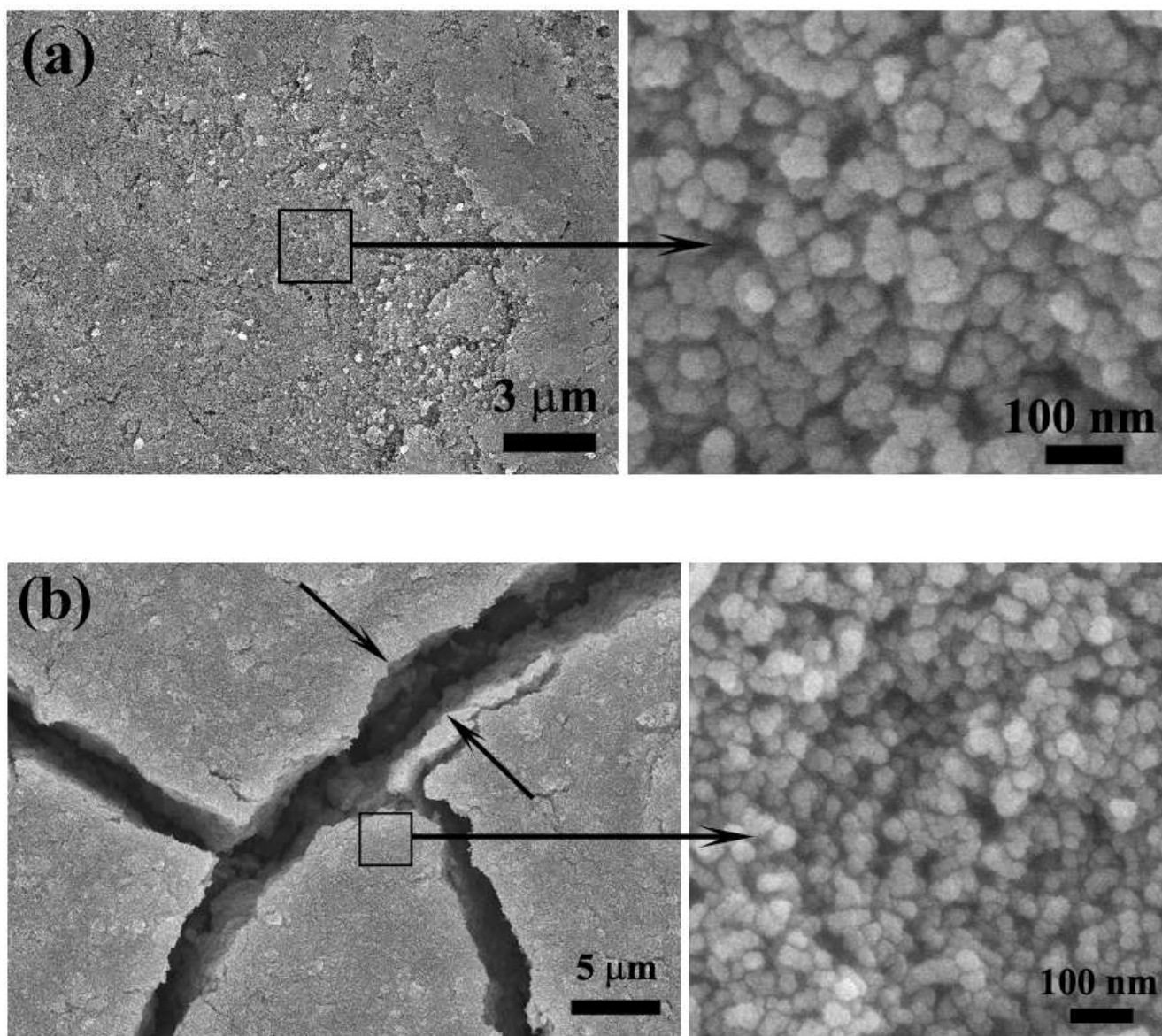


Figure 11. SEM micrographs of ZnO crack-free ((a) sensor S1) and the most cracked ((b) sensor S6) sensing films after annealing and sensing test at 400 C. The squares emphasized the selected regions investigated the size and morphology of particles with the different magnifications.

3.5. Film Thickness Sensing Layer

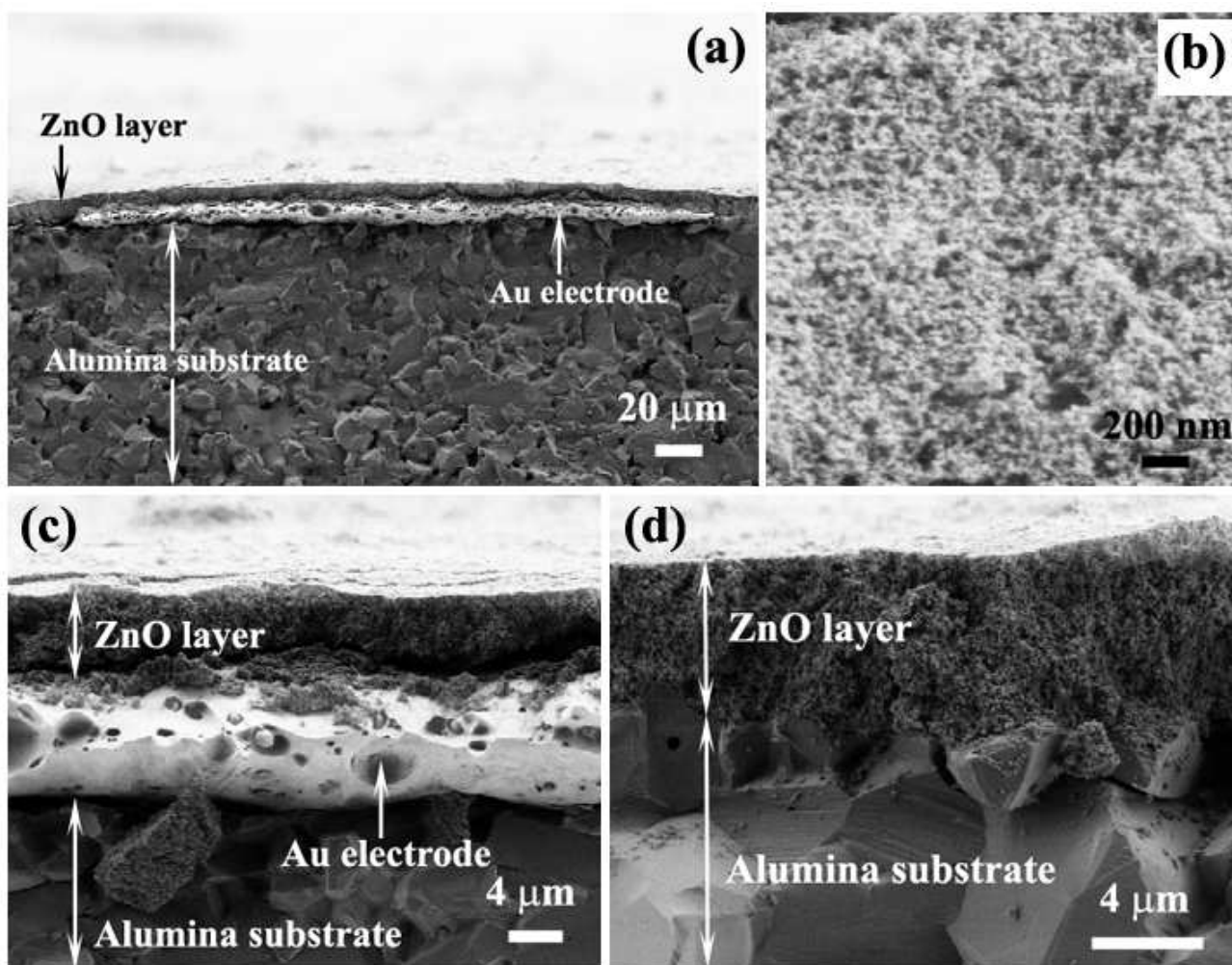


Figure 12. SEM micrographs of flame-made ZnO thick films as a sensor S1 at a different magnifications (side view: a, c, and d) on an Al_2O_3 substrate interdigitated with Au electrodes after annealing and sensing test at 400°C in dry air. The film thickness was approximately $5\ \mu\text{m}$. (top view: b) Regularities in the film thickness and porous sensing film had a crack free.

The cross-section, film thickness, and surface morphology of the sensing film layer (S1) after annealing and sensing test at 400°C were observed using SEM analysis with different magnifications as shown in Fig. 12. The film thickness of sensing film was approximately $5\ \mu\text{m}$ (side view) as shown in Fig. 12 (a), (c), and (d), which benefited tremendously to ethanol gas sensing properties. Regularities in the film thickness (top view) stem from the doctor-blade technique. The sensing film of sensor S1 has a crack-free and a porous structure was formed after annealing process as shown in Fig. 12 (b). The high density Al_2O_3 substrate interdigitated with Au electrodes was also visible.

4. Conclusions

The hexagonal phase of ZnO nanoparticles were made by flame spray pyrolysis of zinc naphthenate in toluene and acetonitrile. The morphologies of ZnO nanoparticles was observed to be mainly spheroidal particles typically with diameters ranging from 10-20 nm with occasional hexagonal and rod-like particles. The crystalline sizes of ZnO hexagonal particles were found to be in the range of 10-20 nm, and nanorod-like particles were found to be ranging from 10-20 nm in width and 20-50 nm in length. Sensing films about 5 μm thick were doctor-bladed onto Al_2O_3 substrate interdigitated with Au electrodes used as the ethanol gas sensors. The gas sensing performances of films were mainly investigated for ppm levels (25-250 ppm) of ethanol with the operating temperature at 400°C. The cracking phenomenon in sensing layer could be improved by varying the heating conditions in terms of the annealing temperature and heating rate. It has been found that the sensor samples annealed using very fast heating rates showed serious cracks than slower heating rates. The sensors had *n*-type response to these vapors with response and recovery times within seconds or minutes, respectively. The crack-free sensor showed higher sensor signal and shorter response time (sensor S1, to 250 ppm, $S=1038$, $T_{\text{res}} = 20$ s) than the most cracked sensor (sensor S6, to 250 ppm, $S=6.9$, $T_{\text{res}} = 40$ s). The recovery times of both types of sensing films (sensor S1 and S6) exhibited quite long within minutes. The sensor characteristics to reducing ethanol gas showed significantly dependence on the heating rates. This is because the heating conditions during annealing process increased and the difference of a thermal expansion coefficient between substrate and material sensing films with increasing crack width which decrease the surface area and connectivity of films and deteriorate film properties of electronic materials. The sensor signal and response time drastically increased and decreased with decreasing crack on sensing layer.

Acknowledgements

The authors gratefully acknowledge the financial support from the Commission on Higher Education, Ministry of Education; the Graduate School, and Nanoscience Research Laboratory (NRL), Department of Chemistry, Faculty of Science, Chiang Mai University, Thailand, and the Particles Technology Laboratory (PTL), Department of Mechanical and Process Engineering, ETH Zentrum, Switzerland for experimental facilities.

References

1. Sahm, T; Mädler, L.; Gurlo, A.; Barsan, N.; Pratsinis, S.E.; Weimar, U. Flame spray synthesis of tin dioxide nanoparticles for gas sensing. *Sens. Actuators B* **2004**, 98, 148-153.
2. Neri, G.; Bonavita, A.; Micali, G.; Donato, N.; Deorsola, F.A.; Mossino, P.; Amato, I.; Benedetti, B.D. Ethanol sensors based on Pt-doped tin oxide nanopowders synthesised by gel-combustion. *Sens. Actuators B* **2006**, 117, 196-204.

3. Li, F.; Xu, J.; Yu, X.; Chen, L.; Zhu, J.; Yang, Z.; Xin, X. One-step solid-state reaction synthesis and gas sensing property of tin oxide nanoparticles. *Sens. Actuators B* **2002**, *81*, 165-169.
4. Rella, R.; Serra, A.; Siciliano, P.; Vasanelli, L.; De, G.; Licciulli, A.; Quirini, A. Tin oxide-based gas sensors prepared by the sol-gel process. *Sens. Actuators B* **1997**, *44*, 462-467.
5. Maekawa, T.; Tamaki, J.; Miura, N.; Yamazoe, N. Development of SnO₂-based ethanol gas sensor. *Sens. Actuators B* **1992**, *9*, 63-69.
6. Gautheron, B.; Labeau, M.; Delabouglise, G.; Schmatz, U. Undoped and Pd-doped SnO₂ thin films for gas sensors. *Sens. Actuators B* **1993**, *15-16*, 357-362.
7. Ivanov, P.; Hubalek, J.; Prášek, K.; Vilanova, X.; Llobet, E.; Correig, X. A route toward more selective and less humidity sensitive screen-printed SnO₂ and WO₃ gas sensitive layers, *Sens. Actuators B* **2004**, *100*, 221-227.
8. Tan, O.K.; Cao, W.; Zhu, W.; Chai, J.W.; Pan, J.S. Ethanol sensors based on nano-sized α -Fe₂O₃ with SnO₂, ZrO₂, TiO₂ solid solutions. *Sens. Actuators B* **2003**, *93*, 396-401.
9. Mädler, L.; Roessler, A.; Pratsinis, S.E.; Sahm, T.; Gurlo, A.; Barsan, N.; Weimar, U. Direct formation of highly porous gas-sensing films by in situ thermophoretic deposition of flame-made Pt/SnO₂ nanoparticles. *Sens. Actuators B* **2005**, *114*(1), 283-295.
10. Park, S.S.; Zheng, H.; Mackenzie, J.D. Ethanol gas sensing properties of SnO₂-based thin-film sensors prepared by the sol-gel process. *Mater. Lett.* **1993**, *17*, 346-352.
11. Ge, J.P.; Wang, J.; Zhang, H.X.; Wang, X.; Peng, Q.; Li, Y.D. High ethanol sensitive SnO₂ microspheres. *Sens. Actuators B* **2006**, *113*, 937-943.
12. Xiangfeng, C.; Caihong, W.; Dongli, J.; Chenmou, Z. Ethanol sensor based on indium oxide nanowires prepared by carbothermal reduction reaction. *Chem. Phys. Lett.* **2004**, *399*, 461-464.
13. Makhija, K.K.; Ray, A.; Patel, R.M.; Trivedi, U.B.; Kapse, H.N. Indium oxide thin film based ammonia gas and ethanol vapour sensor. *Bull. Mater. Sci.* **2005**, *28*, 9-17.
14. Teleki, A.; Pratsinis, S.E.; Kalyanasundaram, K.; Gouma, P.I. Sensing of organic vapors by flame-made TiO₂ nanoparticles. *Sens. Actuators B* **2006**, *119*, 683-690.
15. Sberveglieri, G.; Comini, E.; Faglia, G.; Atashbar, M.Z.; Wlodarski, W. Titanium dioxide thin films prepared for alcohol microsensor applications. *Sens. Actuators B* **2000**, *66*, 139-141.
16. Mabrook, M.; Hawkins, P. A rapidly-responding sensor for benzene, methanol and ethanol vapours based on films of titanium dioxide dispersed in a polymer operating at room temperature. *Sens. Actuators B* **2001**, *75*, 197-202.
17. Ruiz, A.M.; Cornet, A.; Morante, J.R. Performances of La-TiO₂ nanoparticles as gas sensing material. *Sens. Actuators B* **2005**, *111-112*, 7-12.
18. Galatsis, K.; Li, Y.X.; Wlodarski, W.; Comini, E.; Sberveglieri, G.; Cantalini, C.; Santucci, S.; Passacantando, M. Comparison of single and binary oxide MoO₃, TiO₂ and WO₃ sol-gel gas sensors. *Sens. Actuators B* **2002**, *83*, 276-280.
19. Ferroni, M.; Guidi, V.; Martinelli, G.; Roncarati, G.; Comini, E.; Sberveglieri, G.; Vomiero, A.; Della Mea, G. Coalescence inhibition in nanosized titania films and related effects on chemoresistive properties towards ethanol. *J. Vac. Sci. Technol. B* **2002**, *20* (2), 523-530.

20. Zhang, J.; Liu, J.; Peng, Q.; Wang, X.; Li, Y. Nearly monodisperse Cu₂O and CuO nanospheres: Preparation and applications for sensitive gas sensors. *Chem. Mater.* **2006**, *18*, 867-871.
21. Liu, Y.; Dong, J.; Hesketh, P.J.; Liu, M. Synthesis and gas sensing properties of ZnO single crystal flakes. *J. Mater. Chem.* **2005**, *15*, 2316-2320.
22. Xiangfeng, C.; Dongli, J.; Djurišić, A.B.; Leung, Y.H. Gas-sensing properties of thick film based on ZnO nano-tetrapods. *Chem. Phys. Lett.* **2005**, *401*, 426-429.
23. Sahay, P.P.; Tewari, S.; Jha, S.; Shamsuddin, M. Sprayed ZnO thin films for ethanol sensor. *J. Mater. Sci.* **2005**, *40*, 4791-4793.
24. Xu, J.; Chen, Y.; Li, Y.; Shen, J. Gas sensing properties of ZnO nanorods prepared by hydrothermal method. *J. Mater. Sci.* **2005**, *40*, 2919-2921.
25. Wan, Q.; Li, Q.H.; Chen, Y.J.; He, X.L.; Li, J.P.; Lin, C.L.; Wang, T.H. Fabrication and ethanol sensing characteristics of ZnO nanowire gas sensors. *Appl. Phys. Lett.* **2004**, *84*, 3654-3656.
26. Xu, J.; Pan, Q.; Shun, Y.; Tian, Z. Grain size control and gas sensing properties of ZnO gas sensor. *Sens. Actuators B* **2000**, *66*, 277-279.
27. Xu, H.; Liu, X.; Cui, D.; Li, M.; Jiang, M. A novel method for improving the performance of ZnO gas sensors. *Sens. Actuators B* **2006**, *114*, 301-307.
28. Zhu, B.L.; Xie, C.S.; Wang, W.Y.; Huang, K.J.; Hu, J.H. Improvement in gas sensitivity of ZnO thick film to volatile organic compounds (VOCs) by adding TiO₂. *Mater. Lett.* **2004**, *58*, 624-629.
29. Zhu, B.L.; Zeng, D.W.; Wu, J.; Song, W.L.; Xie, C.S. Synthesis and gas sensitivity of In-doped ZnO nanoparticles. *J. Mater. Sci. - Mater. Electron.* **2003**, *14*, 521-526.
30. Rao, B.B. Zinc oxide ceramic semi-conductor gas sensor for ethanol vapour. *Mater. Chem. Phys.* **2000**, *64*, 62-65.
31. Baruwati, B.; Kumar, D.K.; Manorama, S.V. Hydrothermal synthesis of highly crystalline ZnO nanoparticles: A competitive sensor for LPG and EtOH, *Sens. Actuators B* **2006**, *119*, 676-682.
32. Stambolova, I.; Konstantinov, K.; Vassilev, S.; Peshev, P.; Tsacheva, Ts. Lanthanum doped SnO₂ and ZnO thin films sensitive to ethanol and humidity. *Mater. Chem. Phys.* **2000**, *63*, 104-108.
33. Rout, C.S.; Krishna, S.H.; Vivekchand, S.R.C.; Govindaraj, A.; Rao, C.N.R. Hydrogen and ethanol sensors based on ZnO nanorods, nanowires and nanotubes. *Chem. Phys. Lett.* **2005**, *418*, 582-586.
34. Paraguay, F.D.; Yoshida, M.M.; Morales, J.; Solis, J.; Estrada, W.L. Influence of Al, In, Cu, Fe and Sn dopants on the response of thin films ZnO gas sensor to ethanol vapour. *Thin Solid Films* **2000**, *373*, 137-140.
35. Raju, A.R.; Rao, C.N.R. Gas-sensing characteristics of ZnO and copper-impregnated ZnO. *Sens. Actuators B* **1991**, *3*, 305-310.
36. Shen, W.; Zhao, Y.; Zhang, C. The preparation of ZnO based gas-sensing thin films by ink-jet printing method. *Thin Solid Films* **2005**, *483*, 382-387.
37. Xu, J.; Chen, Y.; Chen, D.; Shen, J. Hydrothermal synthesis and gas sensing characters of ZnO nanorods. *Sens. Actuators B* **2006**, *113*, 526-531.

38. Chou, S.M.; Teoh, L.G.; Lai, W.H.; Su, Y.H.; Hon, M.H. ZnO:Al thin film gas sensor for detection of ethanol vapor. *Sensor* **2006**, *6*, 1420-1427.
39. Cheng, X.L.; Zhao, H.; Huo, L.H.; Gao, S.; Zhao, J.G. ZnO nanoparticulate thin film: preparation, characterization and gas-sensing property. *Sens. Actuators B* **2004**, *102*, 248-252.
40. Ge, C.; Xie, C.; Cai, S. Preparation and gas-sensing properties of Ce-doped ZnO thin film sensors by dip-coating. *Mater. Sci. Eng. B* **2007**, *137*, 53-58.
41. Tang, H.; Li, Y.; Zheng, C.; Ye, J.; Hou, X.; Lv, Y. An ethanol sensor based on cataluminescence on ZnO nanoparticles. *Talanta* **2007**, in press.
42. Choopun, S.; Hongstith, N.; Mangkorntong, P.; Mangkornthong, N. Zinc oxide nanobelts by RF sputtering for ethanol sensor. *Physica E* **2007**, in press.
43. Lv, Y.; Guo, L.; Xu, H.; Chu, X. Gas-sensing properties of well-crystalline ZnO nanorods grown by a simple route. *Physica E* **2007**, *36*, 102-105.
44. Zhou, X.; Jiang, T.; Zhang, J.; Wang, X.; Zhu, Z. Humidity sensor based on quartz tuning fork coated with sol-gel-derived nanocrystalline zinc oxide thin film. *Sens. Actuators B* **2006**, in press.
45. Kim, K.W.; Cho, P.S.; Kim, S.J.; Lee, J.H.; Kang, C.Y.; Kim, J.S., Yoon, S.J. The selective detection of C₂H₅OH using SnO₂-ZnO thin film gas sensors prepared by combinatorial solution deposition. *Sens. Actuators B* **2006**, in press.
46. Arshak, K.; Gaidan, I. Development of a novel gas sensor based on oxide thick films. *Mater. Sci. Eng. B* **2005**, *118*, 44-49.
47. Lim, H.J.; Lee, D.Y.; Oh, Y.J. Gas-sensing properties of ZnO thin films prepared by microcontact printing. *Sens. Actuators A* **2006**, *125*, 405-410.
48. Lim, H.J.; Lee, D.Y.; Oh, Y.J. Gas-sensing properties of ZnO thin films prepared by microcontact printing. *Sens. Actuators A* **2006**, *125*, 405-410.
49. Arshak, K.; Gaidan, I. Gas sensing properties of ZnFe₂O₄/ZnO screen-printed thick films. *Sens. Actuators B* **2005**, *111-112*, 58-62.
50. Gao, T.; Wang, T.H. Synthesis and properties of multipod-shaped ZnO nanorods for gas-sensor applications. *Appl. Phys. A* **2005**, *80*, 1451-1454.
51. Feng, X.; Li, Z.J.; Wang, P.; Zhou, Y. Preparation and gas-sensitivity of ultra-fine zinc-oxide powders from roasted zinc-blended. *J. Mater. Sci.* **2005**, *40*, 6597-6600.
52. Gao, T.; Li, Q.; Wang, T. Sonochemical synthesis, optical properties, and electrical properties of core/shell-type ZnO nanorod/CdS nanoparticle composites. *Chem. Mater.* **2005**, *17*, 887-892.
53. Feng, P.; Wan, Q.; Wang, T.H. Contact-controlled sensing properties of flowerlike ZnO nanostructure. *Appl. Phys. Lett.* **87**, 213111-213113.
54. Liewhiran, C.; Phanichphant, S. Influence of thickness on ethanol sensing characteristics of doctor-bladed thick film from flame-made ZnO nanoparticles. *Sensors*, **2007**, *7*, 185-201.
55. Liewhiran, C.; Seraphin, S.; Phanichphant, S. Synthesis of nano-sized ZnO powders by thermal decomposition of zinc acetate using *Broussonetia papyrifera* (L.) Vent pulp as a dispersant. *Curr. Appl. Phys.* **2006**, *6*, 499-502.

56. Purica, M.; Budianu, E.; Rusu, E.; Danila, M.; Gavrilă, R. Optical and structural investigation of ZnO thin films prepared by chemical vapor deposition (CVD). *Thin Solid Films* **2002**, 403-404, 485-488.
57. Dayan, N.J.; Karekar, R.N.; Aiyer, R.C.; Sainkar, S.R. Effect of film thickness and curing temperature on the sensitivity of ZnO:Sb thick-film hydrogen sensor. *J. Mater. Sci. - Mater. Electron.* **1997**, 8, 277-279.
58. Zheng, L.; Xu, T.; Li, G.; Yin, Q. Influence of thickness on oxygen-sensing properties of TiO₂ thin films on Al₂O₃. *Jpn. J. Appl. Phys., Part 1* **2002**, 41, 4655-4658.
59. Lee, Y.L.; Sheu, C.Y.; Hsiao, R.H. Gas sensing characteristics of copper phthalocyanine films; effects of film thickness and sensing temperature. *Sens. Actuators B* **2004**, 99, 281-287.
60. Hossein-Babari, F.; Orvatina, M. Analysis of thickness dependence of the sensitivity in thin film resistive gas sensors. *Sens. Actuators B* **2003**, 89, 256-261.
61. Geistlinger, H. Electron theory of thin-film gas sensors. *Sens. Actuators B* **1993**, 17, 47-60.
62. López, M.A.R.; Peiteado, M.; Fernández, J.F.; Caballero, A.C.; Holc, J.; Drnovsek, S.; Kuscer, D.; Macek, S.; Kosec, M. Thick film ZnO based varistors prepared by screen printing. *J. Eur. Ceram. Soc.* **2006**, 26, 2985-2989.
63. Chang, J.F.; Kuo, H.H.; Leu, I.C.; Hon, M.H. The effects of thickness and operation temperature on ZnO:Al thin film CO gas sensor. *Sens. Actuators B* **2002**, 84, 258-264.
64. Christoulakis, S.; Suche, M.; Koudoumas, E.; Katharakis, M.; Katsarakis, N.; Kiriakidis, G. Thickness influence on surface morphology and ozone sensing properties of nanostructured ZnO transparent thin films grown by PLD. *Appl. Surf. Sci.* **2006**, 252, 5351-5354.
65. Sakai, G.; Baik, N.S.; Miura, N.; Yamazoe, N. Gas sensing properties of tin oxide thin films fabricated from hydrothermally treated nanoparticles dependence of CO and H₂ response on film thickness. *Sens. Actuators B* **2001**, 77, 116-121.
66. Na, D.M.; Satyanarayana, L.; Choi, G.P.; Shin, Y.J.; Park, J.S. Surface morphology and sensing property of NiO-WO₃ thin films prepared by thermal evaporation. *Sensors* **2005**, 5, 519-528.
67. Mueller, R.; Mädler, L.; Pratsinis, S.E. Nanoparticle synthesis at high production rates by flame spray pyrolysis. *Chem. Eng. Sci.* **2003**, 58, 1969-1976.
68. Mädler, L. Liquid-fed aerosol reactors for one-step synthesis of nano-structured particles. *KONA* **2004**, 22, 107-120.
69. Wegner, K.; Stark, W.J.; Pratsinis, S.E. Flame-nozzle synthesis of nanoparticles with closely controlled size, morphology and crystallinity. *Mater. Lett.* **2002**, 55, 318-321.
70. Mädler, L.; Kammler, H.K.; Mueller, R.; Pratsinis, S.E. Controlled synthesis of nanostructured particles by flame spray pyrolysis. *J. Aeros. Sci.* **2002**, 33, 369-389.
71. Kammler, H.K.; Mädler, L.; Pratsinis, S.E. Flame synthesis of nanoparticles. *Chem. Eng. Tech.* **2001**, 24, 583-596.
72. Mädler, L.; Stark, W.J.; Pratsinis, S.E. Rapid synthesis of stable ZnO quantum dots, *J. Appl. Phys.* **2002**, 92, 6537-6540.

73. Tani, T.; Mädler, L.; Pratsinis, S.E. Homogeneous ZnO nanoparticles by flame spray pyrolysis. *J. Nanopart. Res.* **2002**, *4*, 337-343.
74. Height, M.J.; Mädler, L.; Krumeich, F.; Pratsinis, S.E. Nanorods of ZnO made by flame spray pyrolysis. *Chem. Mater.* **2006**, *18*, 572-578.
75. Height, M.J.; Pratsinis, S.E.; Mekasuwandumrong, O.; Praserttham, P. Ag-ZnO catalysts for UV-photodegradation of methylene blue. *Appl. Catal., B* **2005**, *63*, 305-312.
76. Kaelin, M.; Zogg, H.; Tiwari, A.N.; Wilhelm, O.; Pratsinis, S.E.; Meyer, T.; Meyer, A. Electro sprayed and selenized Cu/In metal particles films. *Thin Solid Films* **2004**, *457*, 391-396.
77. Kaelin, M.; Rudmann, D.; Tiwari, A.N. Low cost processing of CIGS thin film solar cells. *Sol. Energy* **2004**, *77*, 749-756.
78. Fortunato, E.; Nunes, P.; Marques, A.; Costa, D.; Águas, H.; Ferreira, I.; Costa, M.E.V.; Godinho, M.H.; Almeida, P.L.; Borges, J.P.; Martins, R. Transparent, conductive ZnO:Al thin film deposited on polymer substrates by RF magnetron sputtering. *Surf. Coat. Technol.* **2002**, *151-152*, 247-251.
79. Yamada, Y.; Kawashima, J.; Wen, J.G.; Niiori, Y.; Hirabayashi, I. Evaluation of thermal expansion coefficient of twinned $\text{YBa}_2\text{Cu}_3\text{O}_{7-\delta}$ film for prediction of crack formation on various substrates. *Jpn. J. Appl. Phys.* **2000**, *39*, 1111-1115.
80. Gopaul, J.; Maskell, W.C.; Pitt, K.E. Plasma oxygen sensor Part I: Effect of crazing of a zirconia thick film on an alumina substrate. *J. Appl. Electrochem.* **1999**, *29*, 93-100.
81. Deesirapipat, Y.; Fujita, M.; Sasajima, M.; Suzuki, R.; Antarasena, C.; Horikoshi, Y. Effect of MgO-buffer layer on the structural and optical properties of polycrystalline ZnO films grown on glass substrate. *Jpn. J. Appl. Phys.* **2005**, *44*, 5150-5155.
82. Kawashima, J.; Yamada, Y.; Hirabayashi, I. Critical thickness and effective thermal expansion coefficient of YBCO crystalline film. *Physica C* **1998**, *306*, 114-118.
83. Kono, A.; Hosoda, H.; Fusayama, T. Heating rate of a gypsum investment related to crack formation. *Shofu Cristobalite Investment B* **1965**, *650*, 1419-1423.
84. Bordia, R.K.; Jagota, A. Crack growth and damage in constrained sintering films. *J. Am. Ceram. Soc.* **1993**, *76*(10), 2475-2485.
85. Cheary, R.W.; Coelho, A.A. Axial divergence in a conventional X-ray powder diffractometer. I. Theoretical foundations. *J. Appl. Crystallogr.* **1998**, *31*, 851-861.
86. Brunauer, S.; Emmett, P.; Teller, P.H. Adsorption of gases in multimolecular layers. *J. Am. Chem. Soc.* **1938**, *60*, 309-319.
87. Liu, Z.; Chung, D.D.L. Burnout of the organic vehicle in an electrically conductive thick-film paste. *J. Elec. Mater.* **2004**, *33*, 1316-1325.
88. Krishnan, B.; Nampoore, V.P.N. Screen printed nanosized ZnO thick film. *Bull. Mater. Sci.* **2005**, *28*, 239-242.
89. Kim, C.J.; Kim, K.B.; Kuk, I.H.; Hong, G.W.; Park, S.D.; Yang, S.W.; Shin, H.S. Fabrication and properties of $\text{YBa}_2\text{Cu}_3\text{O}_{7-\delta}$ -Ag composite superconducting wires by plastic extrusion technique. *J. Mater. Sci.* **1997**, *32*, 5233-5242.

90. Kim, K.B.; Song, Y.H.; Hwang, C.S.; Chung, C.H.; Lee, J.H.; Choi, I.S.; Park, J.H. Efficient electron emissions from printed carbon nanotubes by surface treatments. *J. Vac. Sci. Technol. B* **2004**, *22*, 1331-1334.
91. Li, J.; Nakazato, T.; Kato, K. Effect of cohesive powders on the elutriation of particles from a fluid bed. *Chem. Eng. Sci.* **2004**, *59*, 2777-2782.
92. Wang, T.J.; Jin, Y.; Tsutsumi, A.; Wang, Z.; Cui, Z. Energy transfer mechanism in a vibrating fluidized bed. *Chem. Eng. J.* **2000**, *78*, 115-123.
93. Kisi, E.H.; Elcombe, M.M. *u* Parameters for the wurtzite structure of ZnS and ZnO using powder neutron diffraction. *Acta Crystallogr., Sect. C: Cryst. Struct. Commun.* **1989**, *45*, 1867-1870.
94. Abrahams, S.C.; Bernstein, J.L. Remeasurement of the structure of hexagonal ZnO. *Acta Crystallogr., Sect. B: Struct. Sci.* **1969**, *25*, 1233-1236.
95. Liu, R.S.; Shi, W.C.; Cheng, Y.C.; Huang, C.Y. Crystal structures and peculiar magnetic properties of alpha- and gamma-(Al₂O₃) powders. *Mod. Phys. Lett. B* **1997**, *11*, 1169-1174.
96. Swanson, H.E.; Tatge, E. Standard X-ray diffraction powder patterns. *National Bureau of Standards* **1953**, 359, 1-1, *Zeitschrift fuer Angewandte Physik* **1956**, *8*, 202-205.
97. Cullity, B.D. *Structure of polycrystalline aggregates; Elements of X-ray diffraction*, Addison-Wesley: Massachusetts, 1978; Vol. 2, Chapter 9, p 284.
98. Garman, R.M. *Sintering Theory and Practice*; A Wiley-Interscience: John Wiley & Sons, Inc.; New York, 1996; Chapter 6, p 261.
99. Schierbaum, K.D. Application of organic supramolecular and polymeric compounds for chemical sensors. *Sens. Actuators B* **1994**, *18-19*, 71-76.